A systematic bias in DTI findings

Authors:
Farshid Sepehrband[1, *], Ryan P Cabeen[1], Jeiran Choupan[1, 2], Giuseppe Barisano[1], Meng Law[1, 3], Arthur W Toga[1], for the Alzheimer's Disease Neuroimaging Initiative

Affiliations:
1. Laboratory of Neuro Imaging, USC Stevens Neuroimaging and Informatics Institute, Keck School of Medicine, University of Southern California, Los Angeles, USA
2. Department of Psychology, University of Southern California, Los Angeles, USA
3. Department of Radiology, Keck School of Medicine, University of Southern California, Los Angeles, CA, USA

*** Correspondence to:**
Farshid Sepehrband, PhD
Laboratory of Neuro Imaging,
USC Mark and Mary Stevens Neuroimaging and Informatics Institute,
Keck School of Medicine of USC, University of Southern California,
Los Angeles, CA, USA
T: (+1) 323-442-7246
E: farshid.sepehrband@loni.usc.edu

Keywords: diffusion tensor imaging, bias, perivascular space
Word count: 2585

Data used in preparation of this article were obtained from the Alzheimer's Disease Neuroimaging Initiative (ADNI) database (adni.loni.usc.edu). As such, the investigators within the ADNI contributed to the design and implementation of ADNI and/or provided data but did not participate in analysis or writing of this report. A complete listing of ADNI investigators can be found at: http://adni.loni.usc.edu/wp-content/uploads/how_to_apply/ADNI_Acknowledgement_List.pdf

Abstract

Diffusion tensor imaging (DTI) has been extensively used to map changes in brain tissue related to neurological disorders. Among the most widespread DTI findings are increased mean diffusivity and decreased fractional anisotropy of white matter tissue in neurodegenerative diseases. We show that unincorporated anisotropic free water in perivascular space (PVS) significantly, and systematically, biases DTI measures, casting new light on the biological validity of many previously reported findings. Despite the challenge this poses for interpreting these past results, our findings suggest a new opportunity for incorporating the PVS contribution into diffusion MRI metrics of tissue changes, ultimately strengthening the clinical and scientific value of diffusion MRI.

Introduction

Diffusion MRI is sensitive to water displacement, a physical process that is useful for characterizing structural and orientational features of brain tissue [1,2]. Diffusion tensor imaging (DTI) [3] is the most popular diffusion MRI modeling technique which has been widely used to study brain in health and disease [4–9]. Over the past 30 years, many studies reported DTI-derived measures, such as fractional anisotropy (FA) and mean diffusivity (MD), in neurological diseases. A reproduced and well-known example is the observation of increased MD and decreased FA in neurodegenerative disease such as Alzheimer's disease [10–27]. These findings were often interpreted as the outcome of the white matter degeneration which leads to extra free space for water to displace in every direction, and therefore higher MD and lower FA (i.e. DTI findings are often interpreted as the pathological microstructural alterations of the white matter tissue). However, there remain major concerns regarding the validity of the interpretations. Neuronal degeneration is not the only occurring process, and other pathological changes related to increased glia, presence of Tau tangles and amyloid plaques [28], may even hinder water displacement, and plausibly lower water diffusivity.

Perivascular space (PVS), also known as Virchow-Robin space, is a pial-lined, fluid-filled structure that accompany vessels entering (penetrating arteries) or leaving (draining veins) cerebral cortex [29,30]. Due to the expansive vascularity of the brain, PVS occupies a large portion of the cerebral tissue [31] (**Figure 1.a** and **1.b**). PVS volume varies across people, enlarges with aging as brain tissue shrinks, and changes in many neurological diseases [29,32–39]. Structurally speaking, PVS has a microscopic tubular geometry that occupies extra-vascular space, with decreasing diameter as it penetrates deeper into the brain tissue. Therefore, unlike brain tissue, water molecules of PVS freely move in the microscopic scale, yet they are hindered by the vessel and the cerebral tissue in macroscopic scale. High-resolution MRI and post-mortem studies have shown that PVS in white matter has microscopic scale tubular structure with small diameter that was observed throughout the brain [40,41], This morphological characteristics will result in anisotropic water displacement within this compartment. Based on physical properties of water motion and MRI scanner sensitivities, diffusion profile of PVS fluid appears isotropic only when the diameter of the PVS is larger than the amount of water displacement during the diffusion encoding time and becomes anisotropic when the diameter of the PVS decreases in size.

When DTI measures are estimated, the derived measure reflects the diffusion properties of both the tissue and fluid from the PVS. Given the relatively fast diffusivity of the water expected in PVS, even a small portion of PVS in an imaging voxel can have a substantial effect on the

voxel averaged DTI measures, due to the partial volume effect [42]. Our experiments demonstrate that a failure to incorporate this fluid compartment can impose a systematic bias in DTI findings. For example, in a brain tissue with a given DTI characteristic, if the amount of PVS increases (**Figure 1.c**), DTI modeling would result in an increased MD and decreased FA. While disrupted tissue microstructure is often cited when changes in DTI parameters are observed, the bias imposed by changes in PVS fluid provides a hypothetical but compelling alternative explanation for many reported findings in DTI studies of neurodegenerative diseases.

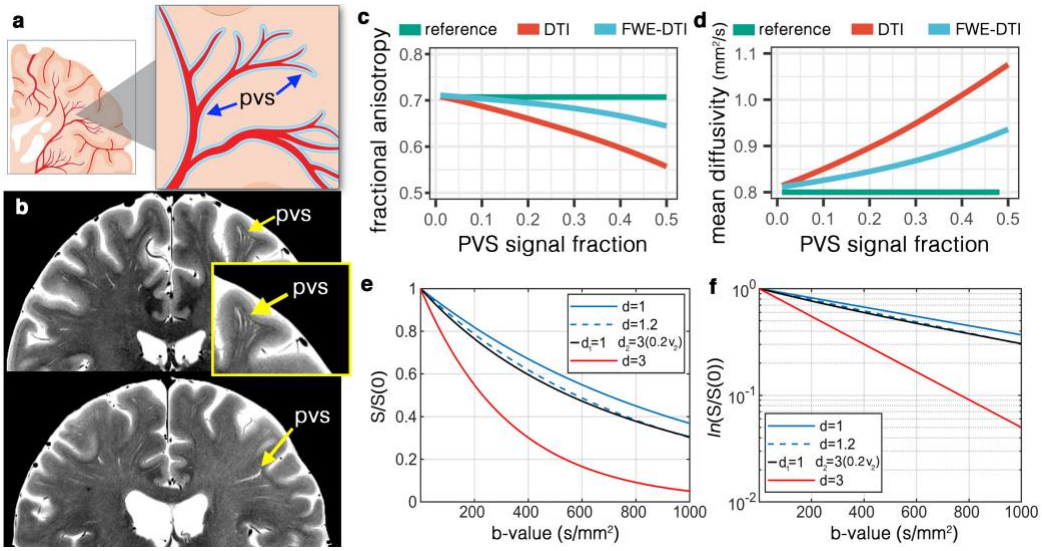

Figure 1. (a) Schematic view of the perivascular space (PVS). **(b)** High-resolution turbo spin echo images of two healthy volunteers (above: 32yr old female, below: 56yr old female), scanned at 7T. In-plane resolution of 0.3mm (interpolated to 0.15mm) was used to acquire the data (with the slice thickness of 2mm). Four averages were acquired to ensure high signal-to-noise ratio. Note that PVS presents throughout the white matter, with larger diameter PVSs closer to the cortex and smaller diameter as it penetrates deep into the white matter. Systematic bias from PVS on DTI was simulated for the mean diffusivity **(c)** and fractional anisotropy **(d)**. As PVS increases the amount of bias amplifies. Free-water elimination (DTI-FWE) technique is also included, which is also affected by PVS presence but to a smaller extent. A plot of diffusion MRI signal for 3 different examples of mean diffusivity (d=1 μm^2/ms, blue line; d=1.2 μm^2/ms, blue dashed line; and d=3 μm^2/ms, red line) is illustrated in **(e)** and the log of the signal is plotted in (**f**). Note that an increased mean diffusivity from 1 μm^2/ms to 1.2 μm^2/ms has a similar signal profile as a scenario with no increased diffusivity but 20% of PVS presence (i.e. PVS signal fraction of 0.2; black line).

Results and Discussion

We simulated diffusion MR signal in a white matter voxel by changing the amount of PVS. Simulation experiments show how FA and MD of the tissue, when modeled using DTI, deviate from the tissue ground truth values, as the amount of PVS increases (**Figure 1.e** and **1.f**). For example, a 20% increase in PVS signal contribution would result in a same signal change if the tissue MD increases from 1 to 1.2 $\mu m^2/ms$. Our simulations show that even a model incorporating an isotropic free water compartment, i.e. without incorporating fluid anisotropy, could still systematically bias results in the same direction as the DTI bias. Although the scale of this bias is significantly lower (**Figure 1.c** and **1.d**).

A remedy to address this bias is to consider two tensors in a voxel [43], one for the tissue and one for the PVS so that both isotropic and anisotropic PVS areas can be modeled. Indeed, the diffusivity of the PVS fluid is higher than the white matter tissue, a prior knowledge which can help separate two compartments in the fitting stage. We used this approach to separate PVS and the tissue. For clarity, the images relating to the tissue are called tissue tensor images (TTI), which were used to investigate the bias of the DTI. DTI reflects the *voxel values*, but TTI reflects *tissue values* and are referred to accordingly. It should be noted that a diffusion MRI acquisition with multiple b-values is required (multi-shell diffusion MRI)[43] for multi-compartment modeling of brain tissue.

We investigated the influence of the PVS on the DTI-derived maps first on a single subject and then on a large cohort of 861 healthy subjects. Subject-level investigation showed that the MD map of DTI was significantly affected by PVS contribution (**Figure 2.a-d)**. Incorporating PVS contribution has dramatically improved the clarity of the MD map (**Figure 2.d**), wherein white matter homogeneity is preserved. Also, the white-gray matter contrast is greater compared with DTI-derived MD. The PVS map visually resembles the T2-weighted image, without the PVS contrast (more examples are provided in **Supplemental Figure 1** and **2**). We observed that ignoring PVS contribution to diffusion MRI signal could even influence the visual presentation of the FA map, particularly around PVS area (**Supplemental Figure 3**).

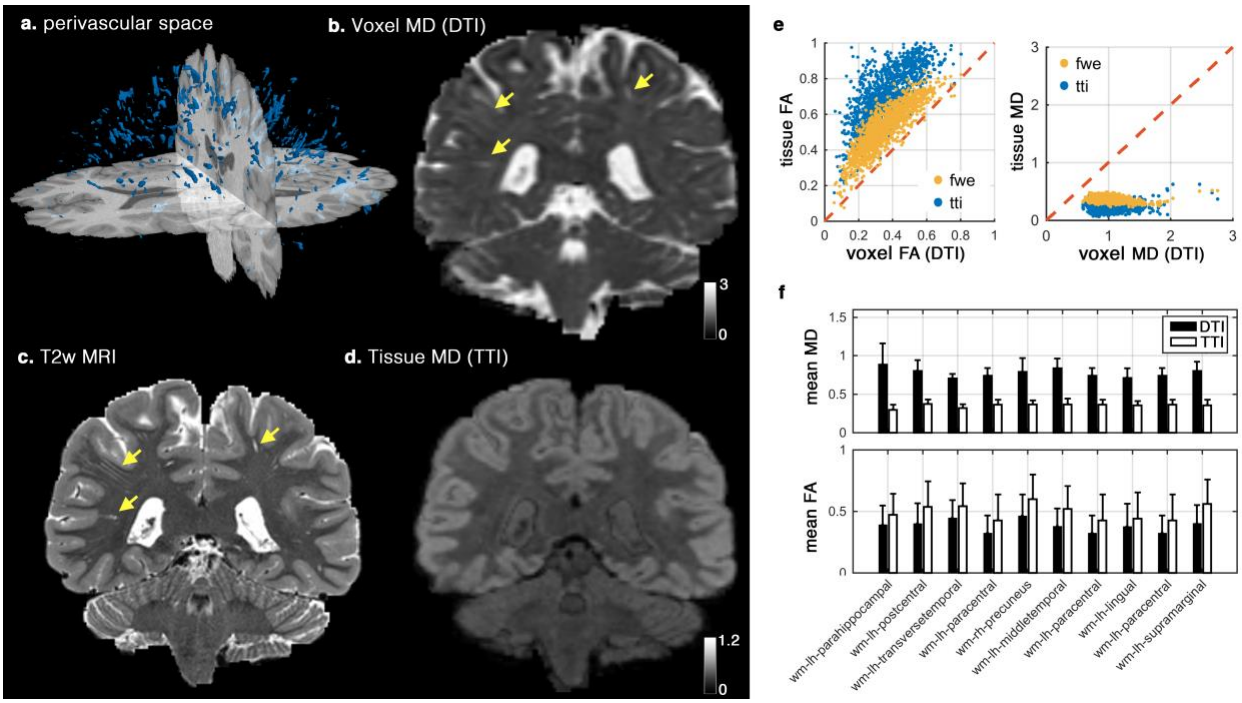

Figure 2. Investigating the effect of the perivascular space (PVS) on DTI in single subject level. Segmented PVS voxels of a healthy subject from human connectome project is plotted in **(a)**. Voxel mean diffusivity (MD), derived using DTI, T2-weighted image and Tissue MD, derived from tissue tensor imaging (TTI) are plotted **(b-d)**, respectively. Note that the expected white matter homogeneity is preserved in tissue MD map, while voxel MD is largely affected by the PVS contribution (extreme cases are demonstrated by yellow arrows). Correlation of the voxel values and the tissue values, derived from DTI and TTI are plotted in **(e)**. Values from free water elimination (FWE) technique are included for comparison. Mean values of MD and FA from DTI and TTI across 10 white matter regions are also plotted **(f)**. All differences of MD and FA mean values in **(f)** are significant at $p<0.001$ (using a paired t-test). Diffusivity values are in $\mu m^2/ms$.

Quantitative MD and FA values from DTI were significantly different from TTI, showing the expected systematic bias of increased MD and decreased FA. **Figure 2.e** shows the correlation of TTI-derived MD and FA with DTI-derived MD and FA. MD values from DTI were significantly higher ($t(1345) = 114.70, p < 0.001$) than tissue MD from TTI. Tissue MD values were more stable compared with voxel MD values ($\frac{std(tMD)}{mean(tMD)} = 0.12$, $\frac{std(vMD)}{mean(vMD)} = 0.22$), reflecting the expected white matter quantitative homogeneity. FA values from DTI were significantly lower in PVS voxels ($t(1345) = -119.55, p < 0.001$). Tissue FA and voxel FA were highly correlated ($r = 0.87, n = 1345, p < 0.001$), but MD values were weakly correlated ($r = 0.15, n = 1345, p < 0.001$). The quantitative difference was observed beyond the PVS voxels and showed to affect the regional values (**Figure 2.f**). Values of all WM regions were significantly different between DTI and TTI (all differences were significant at $p < 0.001$ level).

To determine whether this effect is generalized across individuals, we characterized the DTI bias in a typical adult population by quantitatively examining 861 healthy subjects from human connectome project (HCP) (**Figure 3**) [44]. Empirical results confirmed the simulation study, where an increased MD and a decreased FA in DTI results were observed. Values were compared in PVS voxels and in white matter regions with different expected concentration of PVS, namely: corpus callosum, para-hippocampus, centrum semiovale, and superior-frontal part of the white matter (**Figure 3.c** and **3.f**). When PVS voxels were looked at, a large and significant difference between TTI and DTI measures were observed ($t(860) = 283.13,\ p < 0.001$). Voxel MD values from DTI ($mean = 0.94,\ std = 0.07$) were almost three times higher than TTI values ($mean = 0.39,\ std = 0.02$). This is not surprising given that much of the volume of these voxels are occupied by PVS. MD and FA were also significantly different (all at $p < 0.001$ level) even at region-averaged level across DTI, DTI-FWE and TTI (**Figure 3.c** and **3.f**). FA values derived from DTI-FWE were closer to DTI, but MD values derived from DTI-FWE were closer to TTI, both significantly different (both at $p < 0.001$ level), confirming that DTI-FWE is not a remedy to the PVS imposed bias (detailed statistical report of the **Figure 3** is reported in **Supplemental Note 1**).

Then we specifically examined how the PVS DTI bias affects the study of neurodegeneration using data from the ADNI-3 project [45]. Results from ADNI-3 subjects with multi-shell diffusion MRI data were in-line with simulation and HCP data results (**Figure 4**). It should be noted that voxels of the ADNI-3 diffusion MRI data are 4.1 times larger than that from HCP data, yet the influence of the PVS on the MD map was clearly apparent (**Figure 4.c** and **4.d**). Interestingly, the tissue MD map not only separated PVS from the tissue, but also was able to map the periventricular white matter hyperintensities. MD map of the TTI resembles the FLAIR contrast, with the advantage of having additional quantitative value. To highlight the inter-subject and inter-group variability of the PVS concentration, one example image from each of the CN and MCI groups are demonstrated in **Supplemental Figure 4**.

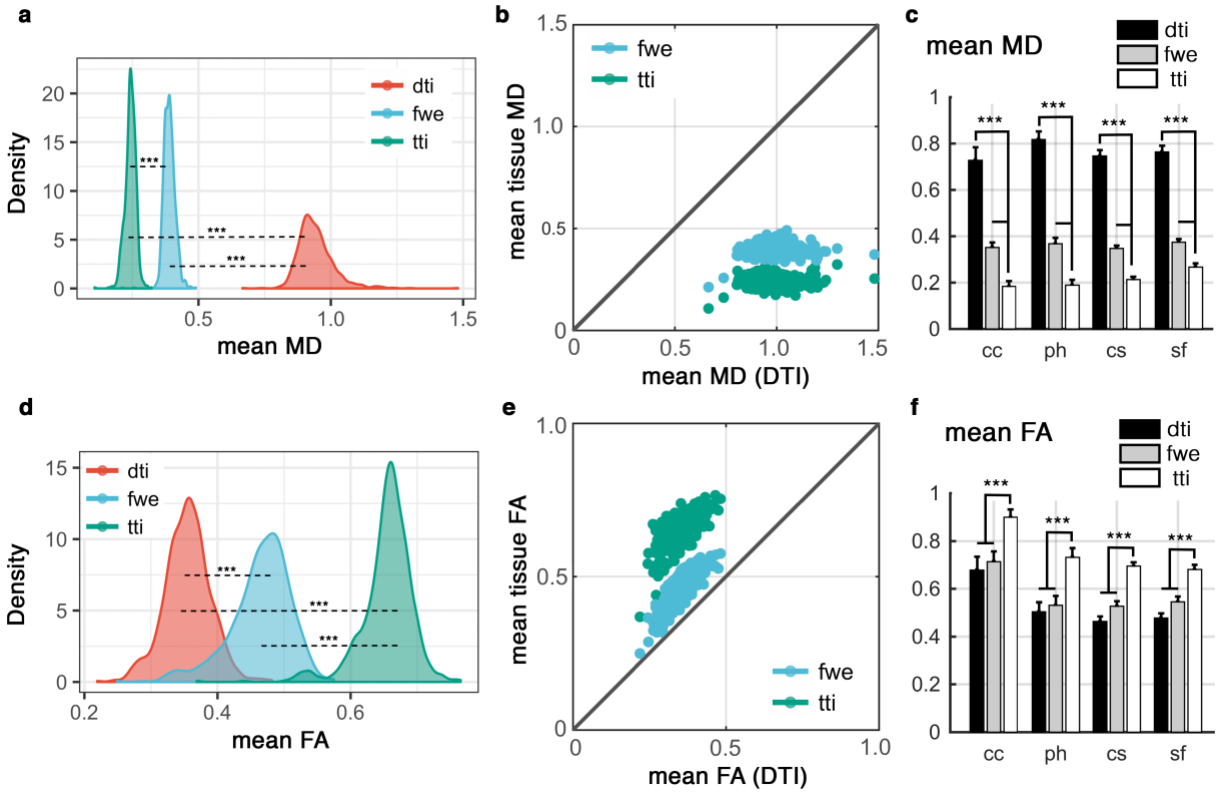

Figure 3. Quantitative investigation of the influence of perivascular space (PVS) on DTI, across 861 subjects of the human connectome project data. Values from DTI were compared with those from free water elimination (FWE) and tissue tensor imaging (TTI) techniques. Mean MD of the PVS voxels are compared in **(a)** and **(b)**. Mean MD values were compared across four white matter regions from Desikan-Killiany atlas **(c)**. Regions are: corpus callosum (cc), para-hippocampus (ph), centrum semiovale (cs) and superior-frontal part of the white matter (sf). All differences are corroborating simulation and subject-level results and are significant at $p<0.001$ (using paired *t*-test)**.** Similar investigation on the fractional anisotropy (FA) values are shown in **(d-f)**. Diffusivity values are in $\mu m^2/ms$.

MD and FA values from DTI were significantly different than those from TTI across all regions of the white matter (20 random regions are plotted in **Figure 4.e** and **4.f**, and the complete list is presented in **Supplemental Figure 5**). The differences were similar to the expected bias and in corroboration with simulation and HCP data analysis. The magnitude of the bias was larger across MD measures compare to FA. The Bland-Altman plots confirms that measures from DTI and TTI are systematically different (MD of DTI is higher, and FA of DTI is lower - **Figure 4.e** and **4.f**).

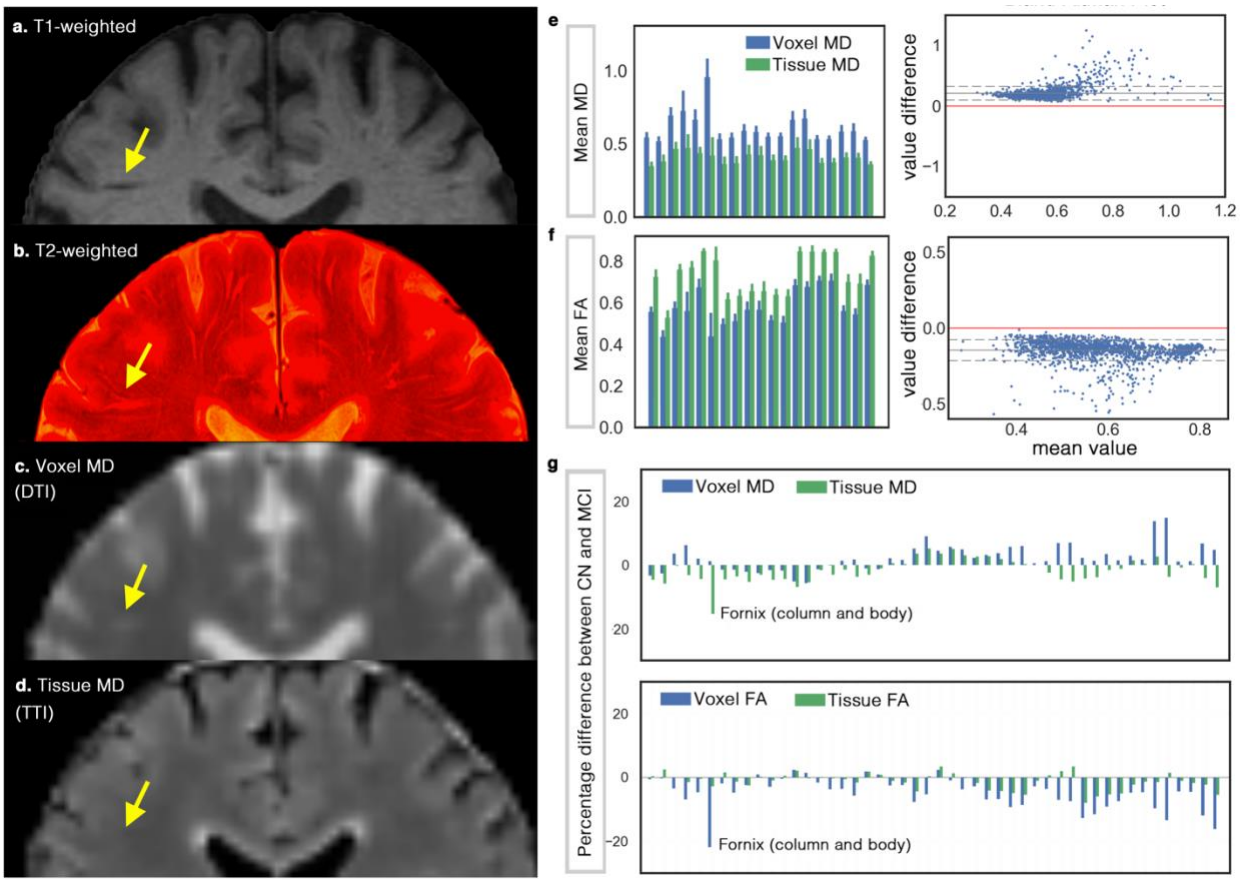

Figure 4. Investigating the effect of perivascular space (PVS) on DTI measures on a cohort of ADNI-3, including 17 cognitively normal (CN) subjects and 16 mild cognitively impaired (MCI) patients. **(a)** shows the T1-weighted, in which a portion of the PVS can be seen. By superimposing high-resolution T2-weighted image on the T1-weighted image **(b)** more PVS are detectable. Mean diffusivity (MD) map from DTI and tissue tensor imaging (TTI) are mapped in **(c)** and **(d)**, respectively. Note that MD from TTI preserved the expected white matter homogeneity by separating the PVS water from the tissue, yet successfully mapped the white matter hyperintensities. White matter hyperintensities are indistinguishable in the MD map from DTI, given the partial volume effect of the periventricular space. Mean voxel MD and tissue MD of 20 randomly selected (for the sake of space) regions from John Hopkins white matter atlas are shown in **(e)**. Bland-Altman plot was drawn to compare DTI versus TTI, which shows the systematic bias of the DTI measures (note that if two techniques were equal the values would show a standard deviation around the value difference of zero, shown by red). **(f)** shows a similar analysis for the fractional anisotropy (FA) measures. The complete chart of John Hopkins white matter regions is illustrated in **Supplemental Figure 5**. **(g)** compares DTI results with TTI when CN group was compared with MCI. Note that for MD, most regions show increased MD (as reported in the literature), but when TTI was used, the inverse pattern was observed in many cases. Fornix is an extreme case of this example (while a large difference in Fornix was observe, it was not statically significant). Diffusivity values are in $\mu m^2/ms$.

An example group-level analysis was performed on the ADNI-3 data to judge if the findings differ when we incorporate a PVS contribution. When comparing MD values of CN and MCI groups using DTI, fifteen regions were significantly different after correcting for multiple comparison using Benjamini–Hochberg procedure [46] and with the false discovery rate of 0.1 (age, sex and brain size were included in the regression). These regions and the statistics are reported in **Supplemental note 2**. When TTI was used, or when the signal fraction of the PVS was included in the regression, none of those regions were significant.

For additional insight, we further investigated one of the regions with significantly different MD value between CN and MCI from the DTI study, namely the superior fronto-occipital fasciculus. Voxel MD (from DTI), tissue MD (from TTI) and PVS signal fraction of this region are plotted in and compared across CN and MCI in **Supplemental Figure 6**. Voxel MD was significantly different between CN and MCI when PVS bias was not considered ($p < 0.01$), however, no significant difference was observed in tissue MD. Interestingly, PVS signal fraction appears to be the main features separating CN and MCI in this region, that is, when it was included as a dependent variable in the regression ($b = 0.0009, t(26) = 4.88, p < 0.001$). When considering all of the regions that we investigated, MD values of DTI were in average 4% higher in the MCI group, but when TTI was used, the MD of the MCI group was in average 2% lower.

When comparing FA values of CN and MCI groups using DTI, eighteen regions were significantly different after correcting for multiple comparison using Benjamini–Hochberg procedure and with the false discovery rate of 0.1 (age, sex and brain size are included in the regression). No region with significant difference was found when TTI was used or when PVS signal fraction was included in the DTI regression model. Only when TTI was used and PVS signal fraction was included in the regression, two regions were weakly significantly different: **1.** Hippocampal connection of the cingulum ($p = 0.0042, \mathrm{FDR}(q) = 0.0043$), **2.** parts of the right sagittal stratum, including inferior longitudinal fasciculus and inferior fronto-occipital fasciculus ($p = 0.0055,\ \mathrm{FDR}(q) = 0.0062$). None of these regions were significantly different with a more conservative false discovery rate (i.e. false discovery rate of 0.05).

Other than PVS fluid, that is physiological in the brain, several pathological features such as cerebral microbleeds and lacunar infarcts, could result in the presence of fluid in the white matter. Such accumulation of fluid, if not modeled, could result to an increased voxel MD. This increase of MD cannot be interpreted as an increased of white matter MD.

It has been shown that by Several techniques and previous studies have included free water in diffusion tensor modeling [43,47–50] or aimed to eliminate it by modifying the imaging sequence [51], mainly to address the CSF partial volume effect around the ventricles. Most of these studies used a fixed-diffusivity isotropic diffusion model and/or treated PVS fluid as a factor to eliminate. Here we emphasize that 1) PVS is not an isotropic compartment and presents throughout the white matter, and 2) Efforts to eliminate fluid contributions may not be the right approach, as parameters obtained from this compartment could be an imaging signal of significant scientific value. For example, Taoka *et al*. recently showed that diffusivity along the perivascular space may reflect impairment of the glymphatic system [52]. The extent to which these findings may be affected by the choice of the model is yet to be examined.

PVS can be mapped with high-resolution T2-weighted imaging only in some voxels where PVS contribution is above the contrast-to-noise ratio [46]. It can however be fully mapped and quantified with diffusion MRI by extracting the signal fraction of the PVS (**Supplemental Figure 1** and **2**). The signal fraction of the PVS and its diffusion characteristics are valuable measures with great potential clinical significance. Microscopic or mesoscopic tissue degeneration may result in microscopic and mesoscopic tissue shrinkage which could change the MRI appearance of the surrounding PVS. Our experiments suggest that diffusion MRI opens a window to characterizing this potentially significant tissue alteration *in vivo*.

Method

Simulation

In the simulation experiments, the diffusion-weighted signal was synthesized with biologically plausible tissue and perivascular space (PVS) contributions. The synthetic model had a baseline signal of one, a fluid signal fraction of 0.1, and axially symmetric and aligned tensors for the tissue and fluid compartments. The tissue compartment had an axial diffusivity of 1.6 $\mu m^2/ms$ and a radial diffusivity of 0.4 $\mu m^2/s$. The fluid compartment had an axial diffusivity of 3.5 $\mu m^2/s$ and a radial diffusivity of 2 $\mu m^2/s$. The signal was simulated using a multi-shell acquisition scheme. Diffusion encoding gradients were optimized for multi-shell sampling, using the *q-space sampling Web application* (http://www.emmanuel-caruyer.com/q-space-sampling.php)[53]. Total of nine shells, with b-values ranging from 0 s/mm^2 to 2000 s/mm^2 were used (at 250 s/mm^2 steps, with 90 q-space sampling per shell). Noise with a standard deviation of 0.025 was added to the simulated signal, then diffusion tensor imaging (DTI) [1,3] and DTI free water elimination (DTI-FWE) [47] models were fitted to the data, and finally diffusion parameters were extracted from the fitted models.

High-resolution 7T images

High-resolution T2-weighted images were acquired to visualize PVS in fine detail. Two healthy adult females (32 and 56 years old) were scanned on a 7 Tesla (7T), whole-body scanner (Terra, Siemens Healthcare, Erlangen, Germany) using a single-channel quadrature transmit radiofrequency (RF) coil and a 32-channel receive array coil (Nova Medical Inc., MA). The institutional review board of the University of Southern California approved the study. Informed consent was obtained from the volunteers, and the image datasets were anonymized.

T2-weighted using turbo-spin echo sequences with in-plane resolution of 300 µm (interpolated to 150 µm) and 2 mm slice thickness were collected. Four averages and two concatenations were acquired to enhance image SNR and CNR [54]. With echo time of 73 ms, repetition time of 3.5 s and total of 25 slices, the acquisition time was 12 minutes.

HCP data and analysis

To evaluate the effect of PVS on DTI measures, we downloaded structural and diffusion magnetic resonance imaging (MRI) data provided by the Human Connectome Project (HCP) [44], namely "S900 release". This dataset includes 861 healthy participants (age, 22–35 years) with multi-shell diffusion MRI (1.25 mm^3 resolution) and structural T1-weighted and T2-weighted images (0.7 mm^3 resolution images), suitable for our analyses. The diffusion MRI image included three shells of b-values (1000, 2000 and 3000 s/mm^2), each with 90 diffusion-weighted images. In addition, 18 non-diffusion-weighted images were acquired.

We used preprocessed data using methods detailed previously, which were preprocessed using HCP pipelines [55–57]. In brief: the structural images were corrected for gradient nonlinearity, readout, and bias field; aligned to AC-PC "native" space and averaged when multiple runs were available; then registered to MNI 152 space using FSL [58]'s FNIRT. The native space images were used to generate individual white and pial surfaces [55] using the FreeSurfer software [59] and the HCP pipelines [55,56]. FSL's TOPUP was used to correct for B0-inhomogeneity distortion using two opposing phase encoded images [60]. FSL's EDDY was used to correct for current induced field inhomogeneity and subject head motion [61], followed by correction for the gradient nonlinearity. Diffusion data were registered to the structural T1-weighted AC-PC space using the non-diffusion-weighted volume. The diffusion gradient vectors were rotated accordingly.

DTI, DTI-FWE and tissue tensor imaging (TTI) models were fitted to HCP subjects using Quantitative Imaging Toolkit (QIT) [62]. For a robust estimation of DTI measure, the shell with the b-value of 1000 s/mm^2 was separated and the tensor model was fitted to each voxel of the

volume using a non-linear least square fitting routine. DTI-FWE model fitting was performed using a custom implementation of the procedure described by Hoy et al. [63], in which the fluid compartment is assigned a constant diffusivity of 3 $\mu m^2/s$ and the optimal signal fraction parameter is determined through a grid search with linear least squares of the tissue tensor compartment at each grid point. The TTI model fitting was performed using constrained trust-region derivative-free optimization using Powell's BOBYQA algorithm [64]. TTI fitting was initialized with the parameters obtained from the DTI-FWE model, and TTI parameters were constrained as follows: the signal fraction was required to be between zero and one, the fluid compartment was required to be axially symmetric fluid compartment with positive diffusivities and have an axis aligned to the tissue principal direction, and the tissue compartment was constrained to be positive definite using a re-parameterization with the Cholesky decomposition.

Diffusion MRI-derived measures were compared in different areas of the white matter: in voxels with high PVS signal fraction and then in four atlas-driven regions of the white matter that are known to have varying PVS appearance in healthy adults [31], namely: corpus callosum (low PVS appearance), para-hippocampus (intermediate PVS appearance), centrum semiovale (high PVS appearance), and superior-frontal part of the white matter (an additional randomly selected region). White matter voxels with high PVS appearance were selected from high-resolution structural images. We noted that the "T1-weighted divided by T2-weighted" images, provided as part of the HCP release, can clearly highlight voxels with high PVS presence. The additional clarity is because fluid appears hyperintense in T2-weighted images and hypointense in T1-weighted images. A threshold of 2.5 (based on manual inspection of the voxels with high PVS presence) was used to segment PVS, where a voxel with "T1-weighted divided by T2-weighted" intensity of smaller than 2.5 was considered a voxel with high PVS presence (**Figure 2.a** is a given example). An inflated mask of ventricle was then used to excluded incorrectly segmented voxels in the periventricular areas, mainly observed in the central and posterior horn of the ventricle. Four white matter regions were extracted from FreeSurfer's white matter segmentation outputs [59], which was derived using Desikan-Killiany atlas [65]. When comparing diffusion MRI-derived measures, paired *t*-test and Pearson correlation was used.

ADNI-3 data and analysis

Data used in the preparation of this article were obtained from the Alzheimer's Disease Neuroimaging Initiative (ADNI) database (http://adni.loni.usc.edu). The ADNI was launched in 2003 as a public-private partnership, led by Principal Investigator Michael W. Weiner, MD. The primary goal of ADNI has been to test whether serial MRI, positron emission tomography (PET),

other biological markers, and clinical and neuropsychological assessment can be combined to measure the progression of mild cognitive impairment (MCI) and early Alzheimer's disease (AD).

The PVS bias was investigated on an Alzheimer disease neuroimaging initiative 3 (ADNI-3) cohort [45], in which multi-shell diffusion MRI data is available. Data from 33 subjects with multi-shell diffusion MRI were downloaded from the ADNI database (http://adni.loni.usc.edu) [66]. Subjects were divided into two groups of cognitively normal (CN) subjects (N=17, 10 females) and MCI patients (N=16, 7 females). Average age of the CN (*M*=76.4, *SD*=7.9) and the MCI group (*M*=74.8, *SD*=6.7) were not statistically different ($t(31)=0.62$, $p=0.53$). The MCI group consists of patients with following cognitive stages: significant memory concerns (N=2), early MCI (N=7), MCI (N=3), late MCI (N=4).

All ADNI-3 images used in this study were acquired using Siemens Prisma or Prisma_fit 3T scanner (Siemens Healthcare, Erlangen, Germany), on six different sites, using a standardized diffusion MRI sequence [67]. Diffusion MRI data was acquired using the following parameters: 2D echo-planar axial imaging, with sliced thickness of 2mm, in-plane resolution of $2mm^2$ (matrix size of 1044 x 1044), flip angle of 90°, 126 diffusion-encoding images with three b-values (6 directions for b-value=500 s/mm^2, 48 directions for b-value=1000 s/mm^2, 60 directions for b-value=2000 s/mm^2), with 13 non-diffusion-weighted images were acquired.

After downloading the raw images, *dcm2nii* was used to convert the *dicom* images to the *nifti* file format [68]. Diffusion MRI were corrected for eddy current distortion and for involuntary movement, using FSL TOPUP and EDDY tools [60,61]. DTI, DTI-FWE, and TTI models were fit using the same procedure as with the HCP data. The data was analyzed using QIT to examine diffusion tensor parameters in deep white matter, as defined by the Johns Hopkins University (JHU) white matter atlas [69]. The JHU regions were segmented in each scan using an automated atlas-based approach described in Cabeen et al., [70] in which deformable tensor-based registration using DTI toolkit (DTI-TK) [71] was used to align the subject data to the Illinois institute of technology (IIT) diffusion tensor template [72], and subsequently transform the JHU atlas regions to the subject data and compute the average of each diffusion tensor parameter with each JHU region.

We used linear regression when investigating the relation between diffusion-derived measures with the cognitive stage using an ordinary least square fitting routine, implemented with the statsmodels.OLS module in Python 3.5.3 (StatsModels version 0.8.0 – other Python packages

that were used are Pandas version 0.20.3 and NumPy version 1.13.1). Multiple regressions were fitted to regional mean values, one region at a time. For every instance, sex, intracranial volume and age were included as covariates. The Benjamini–Hochberg procedure with a false discovery rate of 0.1 was used to correct for multiple comparisons. Diffusion MRI-derived measures were compared using paired *t*-test and Pearson correlation. Bland-Altman plots [73] were used to investigate whether DTI and TTI were systematically different. Bland-Altman plot analysis are designed to investigate a bias between the mean differences [74], where a distribution above or below the 0 (on the y-axis) indicates a bias.

Acknowledgement

This work was supported by NIH grants: 2P41EB015922-21, 1P01AG052350-01 and USC ADRC 5P50AG005142. The content is solely the responsibility of the authors and does not necessarily represent the official views of the NIH.

HCP: Data were provided [in part] by the Human Connectome Project, WU-Minn Consortium (Principal Investigators: David Van Essen and Kamil Ugurbil; 1U54MH091657) funded by the 16 NIH Institutes and Centers that support the NIH Blueprint for Neuroscience Research; and by the McDonnell Center for Systems Neuroscience at Washington University.

ADNI: Data collection and sharing for this project was funded by the Alzheimer's Disease Neuroimaging Initiative (ADNI) (National Institutes of Health Grant U01 AG024904) and DOD ADNI (Department of Defense award number W81XWH-12-2-0012). ADNI is funded by the National Institute on Aging, the National Institute of Biomedical Imaging and Bioengineering, and through generous contributions from the following: AbbVie, Alzheimer's Association; Alzheimer's Drug Discovery Foundation; Araclon Biotech; BioClinica, Inc.; Biogen; Bristol-Myers Squibb Company; CereSpir, Inc.; Cogstate; Eisai Inc.; Elan Pharmaceuticals, Inc.; Eli Lilly and Company; EuroImmun; F. Hoffmann-La Roche Ltd and its affiliated company Genentech, Inc.; Fujirebio; GE Healthcare; IXICO Ltd.; Janssen Alzheimer Immunotherapy Research & Development, LLC.; Johnson & Johnson Pharmaceutical Research & Development LLC.; Lumosity; Lundbeck; Merck & Co., Inc.; Meso Scale Diagnostics, LLC.; NeuroRx Research; Neurotrack Technologies; Novartis Pharmaceuticals Corporation; Pfizer Inc.; Piramal Imaging; Servier; Takeda Pharmaceutical Company; and Transition Therapeutics. The Canadian Institutes of Health Research is providing funds to support ADNI clinical sites in Canada. Private sector contributions are facilitated by the Foundation for the National Institutes of Health (www.fnih.org). The grantee organization is the Northern California Institute for Research and Education, and the study is coordinated by the Alzheimer's Therapeutic Research Institute at the University of Southern California. ADNI data are disseminated by the Laboratory for Neuro Imaging at the University of Southern California.

Reference

1. Bihan, D. Le & Breton, E. *Comptes-Rendus l'Académie des Sci.* **93**, 27–34 (1985).
2. Le Bihan, D. & Johansen-Berg, H. *Neuroimage* **61**, 324–41 (2011).
3. Basser, P.J., Mattiello, J. & LeBihan, D. *Biophys. J.* **66**, 259–267 (1994).
4. Mori, S. & Zhang, J.Y. *Neuron* **51**, 527–539 (2006).
5. Alexander, A.L., Lee, J., Lazar, M. & Field, A.S. *Neurotherapeutics* **4**, 316–329 (2007).
6. Assaf, Y. & Pasternak, O. *J. Mol. Neurosci.* **34**, 51–61 (2008).
7. Horsfield, M.A. & Jones, D.K. *NMR Biomed.* **15**, 570–577 (2002).
8. Sundgren, P.C. et al. *Neuroradiology* **46**, 339–350 (2004).
9. Le Bihan, D. et al. *J. Magn. Reson. Imaging* **13**, 534–546 (2001).
10. Kantarci, K. et al. *JAMA Neurol.* **71**, 1547–1554 (2014).
11. Kantarci, K. et al. *Neurobiol. Aging* **56**, 172–179 (2017).
12. Zhang, Y. et al. *Neurology* **68**, 13–19 (2007).
13. Zhang, Y. et al. *Brain* **132**, 2579–2592 (2009).
14. Amlien, I.K. & Fjell, A.M. *Neuroscience* **276**, 206–215 (2014).
15. Wolf, D., Fischer, F.U., Scheurich, A. & Fellgiebel, A. *J. Alzheimer's Dis.* **47**, 117–127 (2015).
16. Agosta, F. et al. *Radiology* **258**, 853–863 (2011).
17. Mayo, C.D., Mazerolle, E.L., Ritchie, L., Fisk, J.D. & Gawryluk, J.R. *NeuroImage Clin.* **13**, 330–338 (2017).
18. Nir, T.M. et al. *NeuroImage Clin.* **3**, 180–195 (2013).
19. Acosta-Cabronero, J. & Nestor, P.J. *Front. Aging Neurosci.* **6**, 1–21 (2014).
20. Cavedo, E. et al. *Neuroscience* **357**, 119–133 (2017).
21. Charlton, R.A. et al. *Neurology* **66**, 217–222 (2006).
22. Fellgiebel, A. et al. *Dement. Geriatr. Cogn. Disord.* **18**, 101–108 (2004).
23. Naggara, O. et al. *Psychiatry Res. - Neuroimaging* **146**, 243–249 (2006).
24. Kantarci, K. et al. *Neurobiol. Aging* **56**, 172–179 (2017).
25. Westlye, L.T. et al. *Cereb. Cortex* **20**, 2055–2068 (2010).
26. Choi, S.J., Lim, K.O., Monteiro, I. & Reisberg, B. *J. Geriatr. Psychiatry Neurol.* **18**, 12–19 (2005).
27. Sexton, C.E., Kalu, U.G., Filippini, N., Mackay, C.E. & Ebmeier, K.P. *Neurobiol. Aging* **32**, 2322.e5-2322.e18 (2011).
28. Laurent, C., Buee, L. & Blum, D. *Biomed. J.* **41**, 21–33 (2018).
29. Krueger, M. & Bechmann, I. *Glia* **58**, 1–10 (2010).
30. Zhang, E.T., Inman, C.B. & Weller, R.O. *J. Anat.* **170**, 111 (1990).
31. Osborn, A.G. *Diagnostic Surg. Imaging Anat. Brain, Head Neck, Spine* I-16 (2006).
32. Cavallari, M. et al. *J. Neuroimaging* **28**, 273–277 (2018).
33. Brown, R. et al. *Cardiovasc. Res.* cvy113-cvy113 (2018).at <http://dx.doi.org/10.1093/cvr/cvy113>
34. Laveskog, A., Wang, R., Bronge, L., Wahlund, L.-O. & Qiu, C. *Am. J. Neuroradiol.* **39**, 70 LP-76 (2018).
35. Park, L. et al. *Circ. Res.* **121**, 258–269 (2017).
36. Kalaria, R.N. *Neuropharmacology* **134**, 226–239 (2018).
37. Bacyinski, A., Xu, M., Wang, W. & Hu, J. *Front. Neuroanat.* **11**, 101 (2017).

38. Feldman, R.E. et al. *Seizure* **54**, 11–18 (2018).
39. Banerjee, G. et al. *Brain* **140**, 1107–1116 (2017).
40. Bouvy, W.H. et al. *Invest. Radiol.* **49**, 307–313 (2014).
41. Akashi, T. et al. *Am. J. Roentgenol.* **209**, W160–W168 (2017).
42. Alexander, A.L., Hasan, K.M., Lazar, M., Tsuruda, J.S. & Parker, D.L. *Magn. Reson. Med.* **45**, 770–780 (2001).
43. Pierpaoli, C. & Jones, D.K. *Int. Soc. Magn. Reson. Med. Present. ISMRM* 1215 (2004).
44. Essen, D.C. Van et al. *Neuroimage* **80**, 62–79 (2013).
45. Weiner, M.W. et al. *Alzheimer's Dement.* **13**, 561–571 (2017).
46. Kwee, R.M. & Kwee, T.C. *RadioGraphics* **27**, 1071–1086 (2007).
47. Pasternak, O., Sochen, N., Gur, Y., Intrator, N. & Assaf, Y. *Magn. Reson. Med.* **62**, 717–730 (2009).
48. Hoy, A.R. et al. *PLoS One* **12**, 1–21 (2017).
49. Berlot, R., Metzler-Baddeley, C., Jones, D.K. & O'Sullivan, M.J. *Neuroimage* **92**, 27–35 (2014).
50. Metzler-Baddeley, C., O'Sullivan, M.J., Bells, S., Pasternak, O. & Jones, D.K. *Neuroimage* **59**, 1394–1403 (2012).
51. Papadakis, N.G. et al. *Magn. Reson. Med.* **48**, 394–398 (2002).
52. Taoka, T. et al. *Jpn. J. Radiol.* **35**, 172–178 (2017).
53. Caruyer, E., Lenglet, C., Sapiro, G. & Deriche, R. *Magn. Reson. Med.* **69**, 1534–1540 (2013).
54. Sepehrband, F., Wang, D.J.J. & Toga, A.W. *Alzheimer's Assoc. Int. Conf.* (2018).
55. Glasser, M.F. et al. *Neuroimage* **80**, 105–124 (2013).
56. Sotiropoulos, S.N. et al. *Neuroimage* **80**, 125–143 (2013).
57. Milchenko, M. & Marcus, D. *Neuroinformatics* **11**, 65–75 (2013).
58. Jenkinson, M., Beckmann, C.F., Behrens, T.E.J., Woolrich, M.W. & Smith, S.M. *Neuroimage* **62**, 782–790 (2012).
59. Fischl, B. *Neuroimage* **62**, 774–781 (2012).
60. Andersson, J.L.R., Skare, S. & Ashburner, J. *Neuroimage* **20**, 870–888 (2003).
61. Andersson, J.L.R. et al. *Jt. Annu. Meet. ISMRM-ESMRMB* **20**, 2426 (2012).
62. Cabeen, R.P., Laidlaw, D.H. & Toga, A.W. *ISMRM-ESMRMB Abstr.* 12–14 (2014).
63. Hoy, A.R., Koay, C.G., Kecskemeti, S.R. & Alexander, A.L. *Neuroimage* **103**, 323–333 (2014).
64. Powell, M.J.D. *Cambridge NA Rep. NA2009/06, Univ. Cambridge, Cambridge* 26–46 (2009).
65. Desikan, R.S. et al. *Neuroimage* **31**, 968–980 (2006).
66. Toga, A.W. & Crawford, K.L. *Alzheimer's Dement.* **6**, 247–256 (2010).
67. Wyman, B.T. et al. *Alzheimer's Dement.* **9**, 332–337 (2013).
68. Li, X., Morgan, P.S., Ashburner, J., Smith, J. & Rorden, C. *J. Neurosci. Methods* **264**, 47–56 (2016).
69. Mori, S. et al. *Neuroimage* **40**, 570–582 (2008).
70. Cabeen, R.P., Bastin, M.E. & Laidlaw, D.H. *Neuroimage* **146**, 100–112 (2017).
71. Zhang, H., Yushkevich, P.A., Alexander, D.C. & Gee, J.C. *Med. Image Anal.* **10**, 764–785 (2006).
72. Zhang, S., Peng, H., Dawe, R.J. & Arfanakis, K. *Neuroimage* **54**, 974–984 (2011).

73. Altman, D.G. & Bland, J.M. *Stat.* **32**, 307 (1983).
74. Bland, J.M. & Altman, D.G. *Lancet* **346**, 1085–1087 (1995).

Supplemental Figures

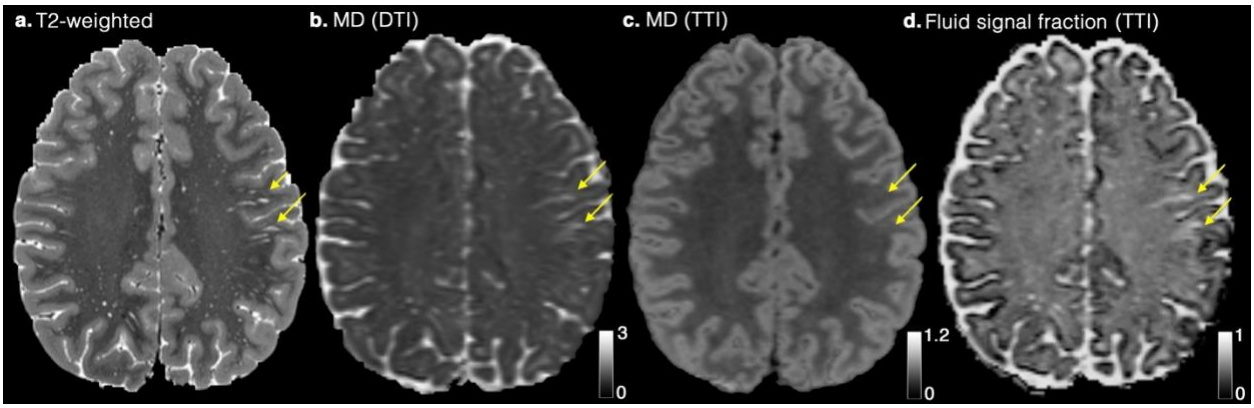

Supplemental Figure 1. An example of the influence of PVS on mean diffusivity (MD) map. (a) T2-weighted image, **(b)** Voxel MD, derived from diffusion tensor imaging (DTI), and **(c)** Tissue MD, derived from tissue tensor imaging (TTI) are shown. **(d)** demonstrates the signal fraction map of the fluid compartment (which includes PVS). Two examples with high PVS concentration are highlighted with yellow arrows. Note that MD from TTI preserves white matter homogeneity and is not affected by PVS contribution, while DTI is significantly affected. MD values are in $\mu m^2/ms$.

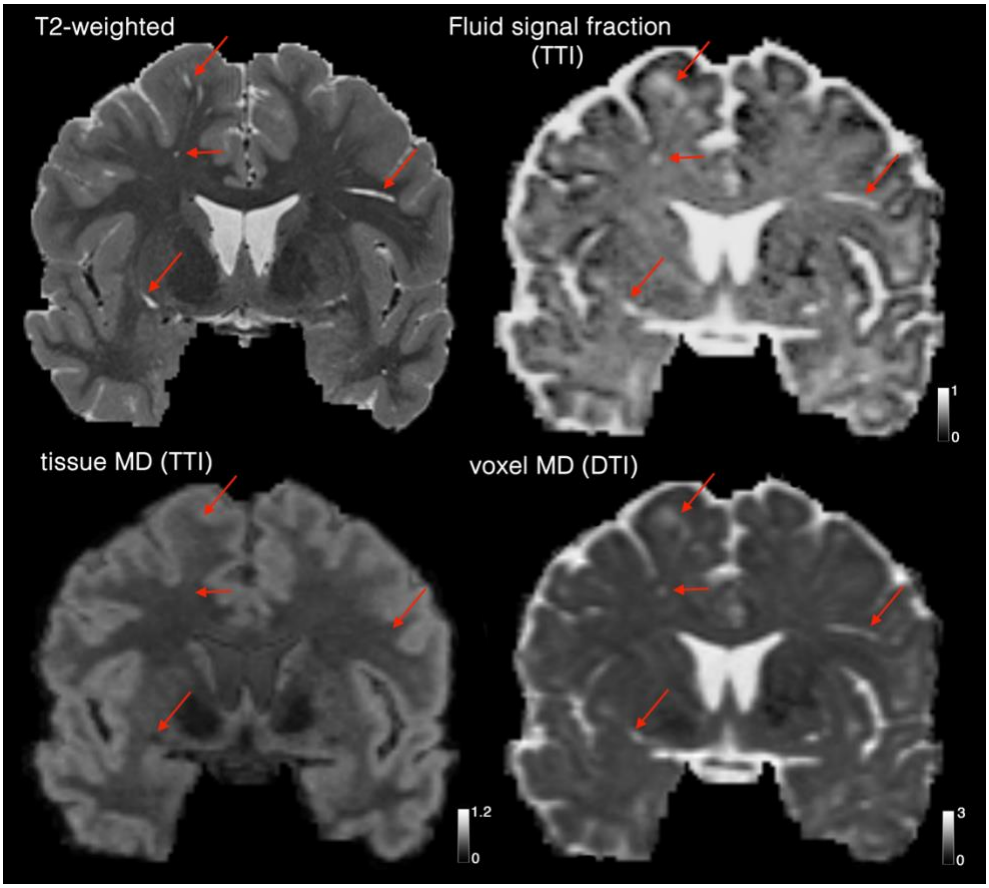

Supplemental Figure 2. Another example of the influence of PVS on mean diffusivity (MD) map, similar to Supplemental Figure 1.

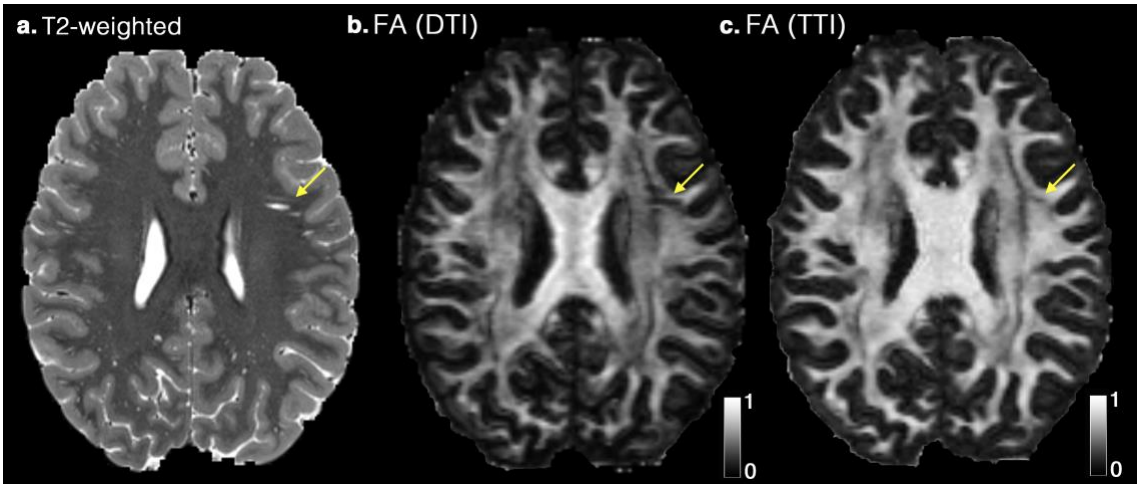

Supplemental Figure 3. An example of the influence of PVS on fractional anisotropy (FA) map. **(a)** T2-weighted image, **(b)** Voxel FA, derived from diffusion tensor imaging (DTI), and **(c)** Tissue FA, derived from tissue tensor imaging (TTI). An example with high amount of PVS is highlighted with yellow arrows. Note that FA values from TTI are higher throughout the brain.

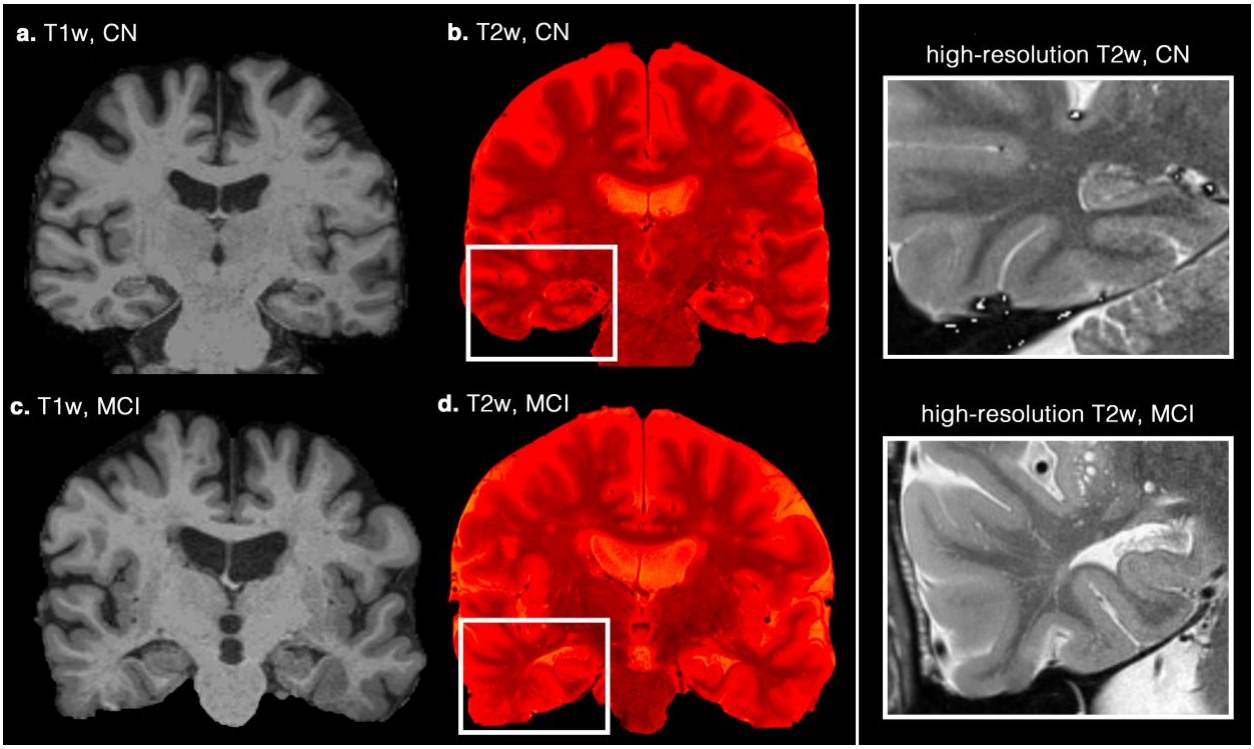

Supplemental Figure 4. Examples of differing perivascular space (PVS) concentration on a cognitively normal (CN) subject and a patient with mild cognitive impairment (MCI) diagnosis. Coronal T1-weighted images (a and c) are illustrated. High-resolution T2-weighted images were superimposed on them to highlight the PVS **(b** and **d)**. Right column figures zoomed into the temporal lobe area, in which increased mean diffusivity and decreased fractional anisotropy are commonly reported. This example does not aim to prove that PVS enlarges in MCI, rather emphasizes on the high inter-subject variability of PVS concentration.

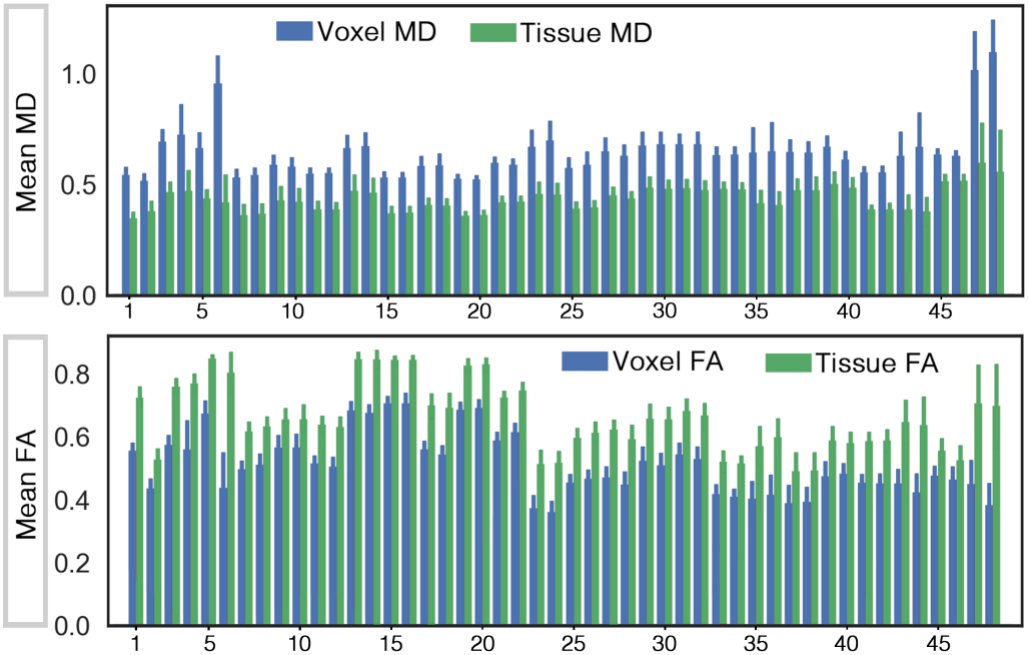

Supplemental Figure 5. Mean and standard deviation of the mean diffusivity (MD) and fractional anisotropy (FA) across regions of the white matter are plotted (*n*=33, from ADNI-3 dataset). Blue bars are voxel values, derived from diffusion tensor imaging (DTI). Green bars are tissue values, derived from tissue tensor imaging (TTI). Diffusivity values are in $\mu m^2/ms$. Mean values of all regions were significantly different between DTI and TTI, at $p<0.001$. Regions are extracted from John-Hopkins white matter atlas: 1. Middle cerebellar peduncle, 2. Pontine crossing tract (a part of MCP), 3. Genu of corpus callosum, 4. Body of corpus callosum, 5. Splenium of corpus callosum, 6. Fornix (column and body of fornix), 7. Corticospinal tract R, 8. Corticospinal tract L, 9. Medial lemniscus R, 10. Medial lemniscus L, 11. Inferior cerebellar peduncle R, 12. Inferior cerebellar peduncle L, 13. Superior cerebellar peduncle R, 14. Superior cerebellar peduncle L, 15. Cerebral peduncle R, 16. Cerebral peduncle L, 17. Anterior limb of internal capsule R, 18. Anterior limb of internal capsule L, 19. Posterior limb of internal capsule R, 20. Posterior limb of internal capsule L, 21. Retrolenticular part of internal capsule R, 22. Retrolenticular part of internal capsule L, 23. Anterior corona radiata R, 24. Anterior corona radiata L, 25. Superior corona radiata R, 26. Superior corona radiata L, 27. Posterior corona radiata R, 28. Posterior corona radiata L, 29. Posterior thalamic radiation (include optic radiation) R, 30. Posterior thalamic radiation (include optic radiation) L, 31. Sagittal stratum (include inferior longitidinal fasciculus and inferior fronto-occipital fasciculus) R, 32. Sagittal stratum (include inferior longitidinal fasciculus and inferior fronto-occipital fasciculus) L, 33. External capsule R, 34. External capsule L, 35. Cingulum (cingulate gyrus) R, 36. Cingulum (cingulate gyrus) L, 37. Cingulum (hippocampus) R, 38. Cingulum (hippocampus) L, 39. Fornix (cres) Stria terminalis (can not be resolved with current resolution) R, 40. Fornix (cres) Stria terminalis (can not be resolved with current resolution) L, 41. Superior longitudinal fasciculus R, 42. Superior longitudinal fasciculus L, 43. Superior fronto-occipital fasciculus (could be a part of anterior internal capsule) R, 44. Superior fronto-occipital fasciculus (could be a part of anterior internal capsule) L, 45. Uncinate fasciculus R, 46. Uncinate fasciculus L, 47. Tapetum R, 48. Tapetum L.

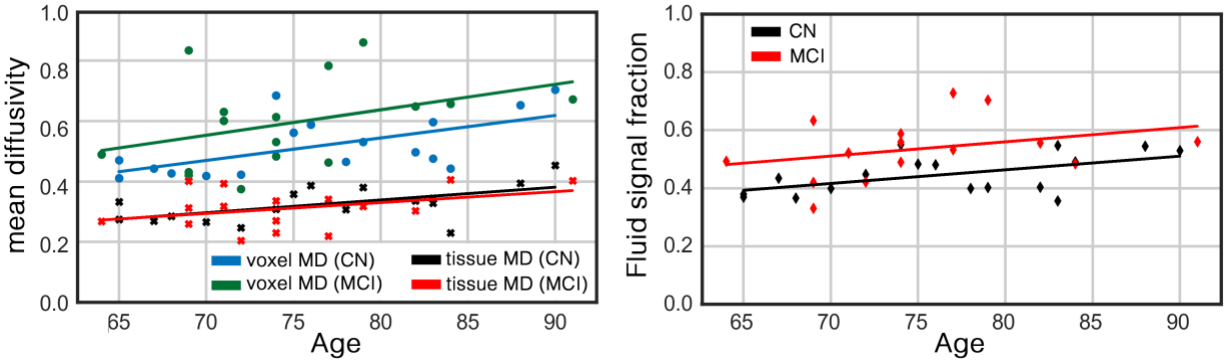

Supplemental Figure 6. An example of a false discovery from of diffusion tensor imaging (DTI) sourced from the PVS bias. Mean diffusivity (MD) of the superior fronto-occipital fasciculus of the cognitively normal (CN) group (n=17) and patients with mild cognitive impairment (MCI) diagnosis (n=16) are plotted in left. Comparison are made using both DTI and tissue tensor imaging (TTI) techniques. From DTI eyes, higher MD was significantly associated with the cognitive stage ($p<0.01$). However, when TTI was used, no difference was observed. PVS signal fraction of this region is plotted in right. The PVS signal fraction had significant association with the cognitive stage ($p<0.001$). Age, sex and brain volume were included in the regression analysis as covariates. Diffusivity values are in $\mu m^2/ms$.

Supplemental note

Supplemental note 1. Comparing mean FA and mean MD as derived from DTI, DTI-FWE and TTI (this supplemental note accompanies **Figure 3** of the manuscript).

Mean FA comparison across HCP subjects:

- FA values from DTI in PVS area were (M = 0.35, SD = 0.03)
- FA values from FWE in PVS area were (M = 0.46, SD = 0.05)
- FA values from TTI in PVS area were (M = 0.65, SD = 0.04)
- FA from TTI was significantly higher than DTI, $t(860) = 313.04$, $p < .001$, and FWE, $t(860) = 119.14$, $p < .001$, techniques.
- FA from FWE was significantly higher than DTI, $t(860) = 129.61$, $p < .001$
- FA was on average 0.3 higher when measured using TTI compare to DTI (almost two times higher).
- FA from TTI was significantly correlated with those from DTI $r(859) = 0.70$, $p < .001$
- FA from TTI was significantly correlated with those from FWE $r(859) = 0.79$, $p < .001$
- FA from FWE was significantly correlated with those from DTI $r(859) = 0.84$, $p < .001$

Mean MD comparison across HCP subjects:

- MD values from DTI in PVS area were (M = 0.94, SD = 0.07)
- MD values from FWE in PVS area were (M = 0.39, SD = 0.02)
- MD values from TTI in PVS area were (M = 0.24, SD = 0.02)
- MD from TTI was significantly higher than DTI, $t(860) = 283.13$, $p < .001$, and FWE, $t(860) = 168.50$, $p < .001$, techniques.
- MD from TTI was on average 0.7 higher than that from DTI (almost four time higher).
- MD from FWE was significantly higher than DTI, $t(860) = 234.86$, $p < .001$
- MD from TTI was weakly correlated with those from DTI $r(859) = -0.06$, $p < .05$
- MD from TTI was correlated with those from FWE $r(859) = 0.25$, $p < .001$
- MD from FWE was correlated with those from DTI $r(859) = 0.11$, $p < .001$

Supplemental note 2. Statistically summary from comparing mean diffusivity (MD) values of DTI of cognitively normal (CN) subjects (*n*=17) and patients with mild cognitive impairment (MCI) diagnosis (*n*=16). Eleven regions were significantly different after correcting for multiple comparison using Benjamini–Hochberg procedure with the false discovery rate of 0.1 (age, sex and brain size were included in the regression). Note that none of these differences were significant after incorporating the contribution of the perivascular space.

White matter region (from John Hopkins WM atlas)	**hemisphere**	***p*-value**	**contrast**	**Is white matter MD different after modeling PVS? (using TTI)**
Anterior limb of internal capsule	Right	0.028	MCI > CN	No
Retrolenticular part of internal capsule	Right	0.012	MCI > CN	No
Retrolenticular part of internal capsule	Left	0.014	MCI > CN	No
Anterior corona radiata	Right	0.013	MCI > CN	No
Anterior corona radiata	Left	0.013	MCI > CN	No
Superior corona radiata	Right	0.013	MCI > CN	No
Superior corona radiata	Left	0.008	MCI > CN	No
Posterior corona radiata	Right	0.010	MCI > CN	No
Posterior corona radiata	Left	0.026	MCI > CN	No
Sagittal stratum (include inferior longitidinal fasciculus and inferior fronto-occipital fasciculus)	Right	0.015	MCI > CN	No
Sagittal stratum (include inferior longitidinal fasciculus and inferior fronto-occipital fasciculus)	Left	0.009	MCI > CN	No
Superior longitudinal fasciculus	Right	0.005	MCI > CN	No
Superior longitudinal fasciculus	Left	0.011	MCI > CN	No
Superior fronto-occipital fasciculus (could be a part of anterior internal capsule)	Right	0.003	MCI > CN	No
Superior fronto-occipital fasciculus (could be a part of anterior internal capsule)	Left	0.013	MCI > CN	No